44th AIAA Aerospace Sciences Meeting and Exhibit
9-12 January 2006, Reno, Nevada

AIAA 2006-767

Plume Characterization of Plasma Thrusters Using Diode-Laser Absorption Spectroscopy

Makoto Matsui*
The University of Tokyo, Chiba, 277-8583, JAPAN

Shigeru Yokota†, Hiroki Takayanagi‡ and Hiroyuki Koizumi§
The University of Tokyo, Tokyo, 133-8656, JAPAN

Kimiya Komurasaki**
The University of Tokyo, Chiba, 277-8583, JAPAN

and

Yoshihiro Arakawa††
The University of Tokyo, Tokyo, 133-8656, JAPAN

Characteristics of a magnetic layer type Hall thruster plume were diagnosed by laser absorption spectroscopy. Translational temperature and number density distributions xenon atom was deduced using an absorption line of XeI 823.16nm. As a result, the temperature was around 430K in the almost all measured region, though it was overestimated at the acceleration channel exit due to the Zeeman effect. The maximum number density was 2.2x10^{19}m^{-3} at the channel exit. Then, the number density decreased by one order at 200mm away from the exit.

Nomenclature

A	=	Einstein coefficient, s^{-1} (pp.2)
A, B	=	hyperfine structure constant, GHz in pp.4
B	=	magnetic flux density, T
C, D	=	function defined in pp. 4
F	=	total angular momentum of whole atom
g	=	statistical weight
h	=	Planck's constant, J.s
I	=	probe laser in4ensity, mW/mm^2 (pp.3) angular momentum of nuclear spin (pp.4,5)
I_0	=	incident laser intensity, mW/mm^2
J	=	total electronic angular momentum
k	=	absorption coefficient, m^{-1}
k_B	=	Boltzmann constant, J/K
K	=	integrated absorption coefficient, GHz m^{-1}
M	=	atomic mass, kg (pp.3) magnetic quantum number (pp.8)
n	=	number density, m^{-3}

* JSPS Research Fellow, Department of Advanced Energy; matsui@al.t.u-tokyo.ac.jp. Member AIAA.
† Graduate student, Department of Aeronautics and Astronutics Student Member AIAA.
‡ Graduate student, Department of Aeronautics and Astronutics Student Member AIAA.
§ Research Associate, Department of Aeronautics and Astronutics Member AIAA.
** Associate Professor, Department of Advanced Energy Member AIAA.
†† Professor, Department of Aeronautics and Astronutics Member AIAA.

P, Q, R	=	function defined in pp. 5
r	=	radial coordinate, mm
R	=	plume radius, mm
T	=	translational temperature, K
T_e	=	electron temperature, eV
v	=	velocity of atom, m/s
x	=	coordinate in the laser pass direction, mm
y	=	probe beam position, mm
z	=	axial coordinate, mm
α^A	=	natural abundance of xenon
$\beta^A_{Fi, Fj}$	=	relative intensity of nuclear spitted line
$\gamma^A_{Fi,Fj}$	=	correction coefficient of Doppler width
ΔE	=	energy gap, eV
ΔE_{NS}	=	energy shift of nuclear spin splitting, eV
λ	=	wavelength, nm
μ_B	=	Bohr magneton, J/T
ν	=	laser frequency, Hz
ν_0	=	center absorption frequency, Hz
$\nu^A_{0, IS}$	=	isotope shift of center absorption frequency, GHz
$\nu^A_{0, Fi, Fj}$	=	nuclear spin shift of center absorption frequency, GHz
ν_{0_AZ}	=	anomalous Zeeman shift, GHz
$\Delta\nu_D$	=	Doppler width, GHz

Subscript

i	=	absorption state
j	=	excited state
tot	=	total states

Superscript

A	=	atomic mass, amu

I. Introduction

Hall thrusters are one of the promising thrusters of satellites for orbit transfer or North/South station keeping missions because it produces high thrust efficiency, exceeding 50%, with a specific impulse range of 1000-3000 s and a higher ion beam density than ion thrusters because of the existence of electrons in the ion acceleration zone. This is because a moderate magnetic field is applied in the acceleration zone, causing the magnetization of the electrons and not the ions.[1-3]. Hence, several types of Hall thrusters are actively developed in Russia, USA, EU and Japan[4-10].

In their practical use in a spacecraft, the interactions between the plume of the thruster and the host spacecraft cause serious problems[11-13]. High-energy main beam ions generated and accelerated in the acceleration channel collide with unionized propellant atoms in the plume, resulting in the production of low-energy ions and high-energy atoms by charge exchange reaction (CEX). These CEX ions propagate in the radial and upstream directions because of the potential distribution near the spacecraft. The backflow of CEX ions becomes a contamination source causing erosion, sputtering, degradation, increment of temperature and potential change of solar arrays or spacecraft surfaces.

Then, it is important to clarify a production mechanism of CEX reactions. Plume characteristics have been a hot subject and investigated experimentally in ground-based facilities[14-20] and even in an actual flight test[21] as well as numerical calculations[22-25]. Because most of measurements, however, are conducted by intrusive probe methods such as electrostatic probes, energy analyzers and mass spectrometers, measurements near the thruster exit are difficult for their disturbances, where CEX reactions would most frequently take place[14-20]. The plume properties near the thruster exit are also useful for initial conditions of numerical calculations.

In this study, laser absorption spectroscopy was applied to a magnetic-layer-type Hall thruster plume developed in the University of Tokyo[9]. Number density and temperature distributions of neutral xenon atom are deduced from measured absorption profiles at 823.16nm ($6s[3/2]^0_2 \rightarrow 6p[3/2]_2$) assuming Boltzmann equilibrium among all excited states.

II. Theory of Laser Absorption Spectroscopy

Laser absorption spectroscopy has some superiority to other non-intrusive spectroscopes such as emission and LIF: 1) it is applicable to optically thick plasma, and 2) absolute calibration using a standard light source or a density reference cell is not necessary. Moreover, 3) the measurement system is portable when a diode laser is used[26]. In this section, a general theory of laser absorption spectroscopy is described and then a hyperfine structure of xenon atom is discussed.

A. Absorption Coefficient and Number Density

The relationship between probe laser intensity I and absorption coefficient $k(x)$ is expressed by the Beer-Lambert law as[27],

$$\frac{\mathrm{d}I}{\mathrm{d}x} = -k(x)I \ . \tag{1}$$

Because distributions of absorption properties in plumes would be axisymmetric, local absorption coefficient $k_\nu(r)$ with the radial coordinate r is obtained by the Abel inversion expressed as[28],

$$k(r) = \frac{1}{\pi}\int_r^R \frac{d(\ln \frac{I}{I_0}(y))}{dy} \frac{dy}{\sqrt{y^2 - r^2}} \ . \tag{2}$$

Assuming Boltzmann relation between absorbing and excited states, integrated absorption coefficient $K(r)$ is expressed as a function of the number density at the absorbing state $n_i(r)$ as[27],

$$K(r) = \int_{-\infty}^{\infty} k_\nu(r)\mathrm{d}\nu = \frac{\lambda^2}{8\pi}\frac{g_j}{g_i}A_{ji}n_i(r)\left[1 - \exp\left(-\frac{\Delta E_{ij}}{k_\mathrm{B}T_\mathrm{e}}\right)\right] . \tag{3}$$

To be exact, g should be corrected from g=2J+1 to g=(2J+1)(2I+1) when nuclear spin has non-zero value. However, Eq. (3) is still valid because both absorbing and excited states have common I[29].

Assuming Boltzmann relations among all excited states, total number density n_tot is deduced from measured number density as,

$$n_\mathrm{tot} = \frac{n_i}{g_i}\sum_l g_l \exp\left(-\frac{\Delta E_{li}}{k_\mathrm{B}T_\mathrm{e}}\right) . \tag{4}$$

Here summation l is taken for all states[30].

B. Line broadening and Translational Temperature

An absorption profile of an atomic line is broadened by various physical mechanisms, and then expressed by a convolution of the Lorentz and the Gauss distributions. However, in low-pressure plasma, Doppler broadening is dominant and the other broadenings such as natural, pressure, Stark broadenings are negligible[26]. Then, in this study, only Doppler broadening is considered.

The proper frequency ν_0 of a moving atom at velocity v is observed to be shifted by the Doppler effect resulting in causing broadening of the profile. This is called the Doppler broadening. This broadening is the Gauss distribution and its full width at half maximum (FWHM) $\Delta\nu_\mathrm{D}$ is related to the translational temperature T as[27],

$$\Delta\nu_D = \frac{2\nu_0\sqrt{\ln 2}}{c}\sqrt{\frac{2k_\mathrm{B}T}{M_A}} \ . \tag{5}$$

Here, c and M_A are velocity of light and atomic mass.

C. Hyperfine Structure

Because xenon atom has a hyperfine structure, line-shape analysis has to be cared[31-34]. The hyperfine structure consists of a combination of isotope shifts and nuclear spin splitting. Here the hyperfine structure of 823.16nm line is described.

1. Isotope shift

Xenon has nine isotopes and their natural abundance α^{A} is tabulated in Table 1[29]. Since each isotope has different mass and nuclear radius, the same transition line of each isotope has a slightly different energy gap. The corresponding shift of center absorption frequency $\nu^{A}_{0,\,IS}$ is the sum of mass effect and field effect. Table 1 also shows the experimental isotope shifts of 823.16nm line taken from References 35, 36. Here the shift is conventionally defined relative to the center frequency of ^{132}Xe and the value is transferred in GHz though the original data is written in mk.

Table 1 Natural abundance of xenon isotopes and isotope shifts of 823.16nm line.

A, amu	124	126	128	129	130	131	132	134	136
α^{A}, %	0.0096	0.090	1.92	26.4	4.1	21.2	26.9	10.4	8.9
$\nu^{A}_{0,\,IS}$, GHz	0.270	0.186	0.114	0.122	0.054	0.080	0	-0.052	-0.149

2. Nuclear spin splitting

As tabulated in Table 1, two isotopes have odd atomic mass. This means that they have non-zero nuclear spin whereas seven isotopes with even atomic mass have not nuclear spin. The nuclear spin of ^{129}Xe is 1/2 and that of ^{131}Xe is 3/2. Then, total angular moment of the whole atom F should be considered by sum of total electronic angular moment J and nuclear spin I, resulting in the splitting of the line. The quantum number of F can take values,

$$F = J + I, J + I - 1, \ldots, |J - I|. \tag{6}$$

The selection rule for F is

$$\Delta F \equiv F_i - F_j = 0, \pm 1. \tag{7}$$

Here, zero-zero transition is forbidden (F=F≠0). Then, ^{129}Xe and ^{131}Xe lines are split into four and ten, respectively. Figure 1 shows a Grotrian diagram and the hyperfine structure of 823.16nm line.

The energy shift of the nuclear spin splitting ΔE_{NS} is the sum of nuclear magnetic dipole and quadrupole interaction expresses as[39],

$$\Delta E_{NS} = \frac{AC}{2} + BD. \tag{8}$$

Here, A is the nuclear magnetic dipole constant and B is the nuclear magnetic quadrupole constant. C and D is the function of F, I and Jdefined as,

$$C = F(F+1) - I(I+1) - J(J+1).$$

$$D = \frac{3C(C+1) - I(I+1)J(J+1)}{8I(2I-1)(2J-1)}. \tag{9}$$

The relative frequency shifts of the nuclear spin splitting to the isotope shift $\nu^{A}_{0,\,Fi,\,Fj}$ are tabulated in Table 2. Here A and B are taken from References 35-38.

The relative intensity of the nuclear spin splitting for J_i=J_j transition are expressed as[39],

$$I(F \to F) \propto \frac{(2F+1)R^2(F)}{F(F+1)}.$$

$$I(F \to F-1, F-1 \to F) \propto \frac{P(F)Q(F-1)}{F}. \tag{10}$$

Here, $P(F)$, $Q(F)$ and $R(F)$ are defined as,

$$\begin{aligned} P(F) &= (F+J)(F+J+1) - I(I+1) \\ Q(F) &= I(I+1) - (F-J)(F-J+1) \\ R(F) &= F(F+1) + J(J+1) - I(I+1) \end{aligned}. \tag{11}$$

Table 2 also shows the relative intensity $\beta^A_{Fi,\,Fj}$. Here the summation of $\beta^A_{Fi,\,Fj}$ for each isotope is normaized to be unity.

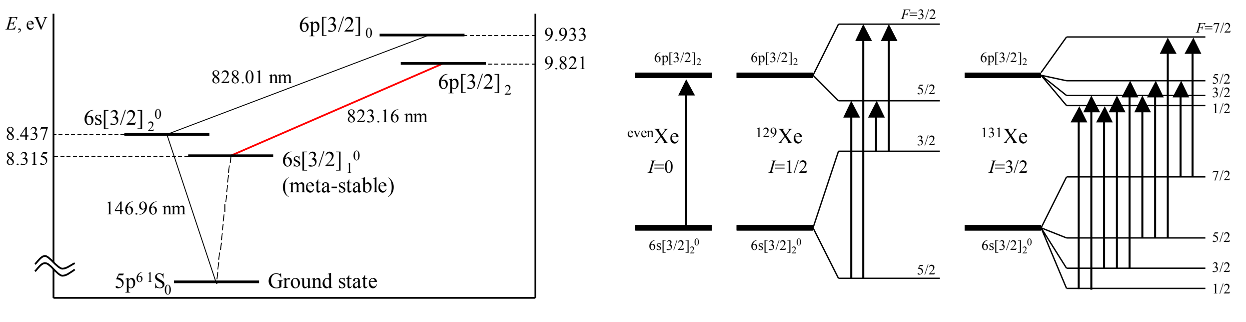

Fig.1 Grotrian diagram (left figure) and hyperfine structure (right figure) of XeI 823.16nm line.

Table 2 Frequency shifts and relative intensity of nuclear spin splitting of 823.16nm.

^{129}Xe, I=1/2, J_i=J_j=2			
F_i	F_j	$\nu^A_{0,\,Fi,\,Fj}$, GHz	$\beta^A_{Fi,\,Fj}$
5/2	5/2	1.492	0.56
5/2	3/2	-4.470	0.04
3/2	5/2	3.724	0.04
3/2	3/2	2.239	0.36

^{131}Xe, I=3/2, J_i=J_j=2			
F_i	F_j	$\nu^A_{0,\,Fi,\,Fj}$, GHz	$\beta^A_{Fi,\,Fj}$
7/2	7/2	-1.381	0.343
7/2	5/2	1.313	0.057
5/2	7/2	-2.334	0.057
5/2	5/2	0.360	0.173
5/2	3/2	1.968	0.07
3/2	5/2	-0.283	0.07
3/2	3/2	1.325	0.08
3/2	1/2	2.164	0.05
1/2	3/2	0.954	0.05
1/2	1/2	1.793	0.05

D. Absorption Profile

Considering the Doppler dominant broadening and the hyperfine structure, the absorption profile is a superposition of twenty-one Gaussian functions whose relative square are determined by natural abundance and relative intensity of the hyperfine structure. Then, the profile is expressed as,

$$k(\nu) = K \sum_{A,F}^{21} \frac{2\alpha^A \beta^A_{F_i,F_j}}{\gamma^A_{F_i,F_j} \Delta\nu_D} \sqrt{\frac{\ln 2}{\pi}} \exp\left[-\ln 2 \left\{ \frac{2\left(\nu - \nu_0 - \nu^A_{0,\mathrm{IS}} - \nu^A_{0,F_i,F_j}\right)}{\gamma^A_{F_i,F_j} \Delta\nu_D} \right\}^2 \right]. \tag{12}$$

Here, $\gamma^A_{Fi,Fj}$ is the correction coefficient of Doppler width. Assuming that translational temperature is independent of the isotopes, Doppler width of each isotope is slightly different from each other due to the difference of mass and center frequency in Eq.(5). Then, $\gamma^A_{Fi,Fj}$ is expressed as,

$$\gamma^A_{F_i,F_j} = \frac{\nu_0^{132} + \nu^A_{0,\mathrm{IS}} + \nu^A_{0,F_i,F_j}}{\nu_0^{132}} \sqrt{\frac{M_{132}}{M_A}}. \tag{13}$$

III. Experimental Setup

A. Magnetic-layer-type Hall thruster

Figures 2 and 3 show a cross section of a magnetic-layer-type Hall thruster and its photo in operation. The inner and outer diameters of the acceleration channel are 48 and 62 mm, respectively. An acceleration channel wall was made of BN. The anode is located at 21 mm, upstream end of the acceleration channel. A solenoid coil is set at the center of the thruster to apply a radial magnetic field in the acceleration channel. The magnetic flux density is varied by changing the coil current. There is no outer coil because a uniform magnetic field distribution is maintained along the azimuthal direction. A hollow cathode (7HCN-001-001; Veeco-Ion Tech Inc.) was used as an electron source and a neutralizer. A vacuum chamber of 2 m diameter by 3 m length was used in the experiments. The pumping system comprised a diffusion pump (37000 *l*/s), a mechanical booster pump (2800 *l* /s), and two rotary pumps (250 *l* /s). An operation condition is tabulated in Table 3.

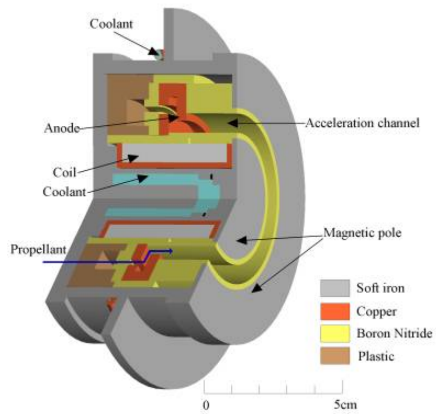

Fig.2 Cross section of a magnetic layer type Hall thruster.

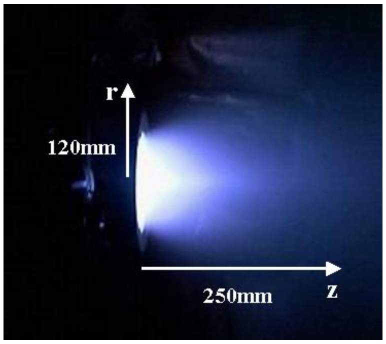

Fig.3 A photo of a Hall thruster plume.

Table 3 Operation conditions.

Parameter	Value
Working gas	Xenon
Mass flow rate	1.0 Aeq (1.36 mg/s)
Discharge voltage	260 V
Discharge current	1.0 A
Applied magnetic field	0.014 T
Ambient pressure	7.8×10^{-3} Pa

B. Measurement System

Figure 4 shows a schematic of the measurement system. A single longitudinal mode diode-laser (HL8325G; HITACHI Ltd., LDC205; Thorlabs Inc.) was used as the laser oscillator. The laser frequency monitored by a spectrometer (PMA50; Hamamatsu Photonics K.K.) was roughly matched to the absorption one by temperature control (TED200; Thorlabs Inc.). Then, it was scanned over the absorption line shape by current modulation with a function generator. The modulation frequency and width were 1 Hz and 30 GHz, respectively. An etalon was used as a fine wave-meter. Its free spectral range was 1 GHz.

The probe beam was guided into the vacuum chamber through a multimode optical fiber. The fiber output was mounted on a two-dimensional traverse stage to scan the plume in the radial and axial direction. Although probe beam diameter was 5 mm, spatial resolution determined by the photo detector area was 1 mm. To reduce plasma emission, a band pass filter, whose FWHM is 10 nm, was used. As a reference, absorption signal in glow discharge plasma was also monitored. Its input power, discharge voltage and ambient pressure were 1.5 mW, 500 V, and xenon 79 Pa, respectively. All signals were recorded using a digital oscilloscope (DL708; Yokogawa Co.) with 10-bit resolution.

Measurement range is r<120 mm and z<250 mm as shown in Fig.3. Here, r and z are the radial and axial coordinates.

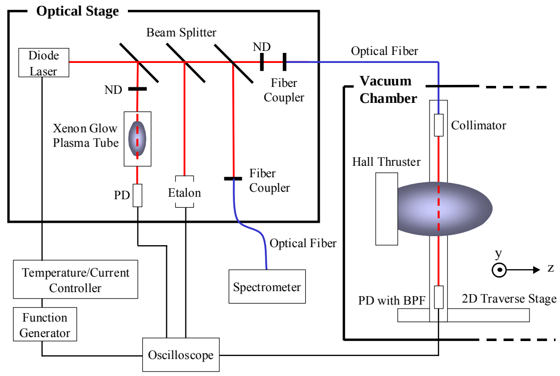

Fig.4 Measurement system.

IV. Results and Discussion

A. Data Processing

Figure 5 shows transmitted laser intensity signals of Hall plume and glow plasma and an etalon signal. At each measurement point, eight profiles were recorded. To obtain absorbance, measured profiles were normalized by the etalon signal and the laser signal without absorption. Then, local absorption profiles were reconstructed by the Abel inversion of the absorbance at every 0.05GHz. Figure 6 shows an absorption profile at z=50mm, r=20mm and relative intensity of the hyperfine structure as a bar graph. The peaks of the hyperfine structure were observed at estimated position in frequency. Figure 6 also shows a curve fitting of Eq.(12). The fitting was well on the measured profile. This shows the validation of Gaussian dominant assumption.

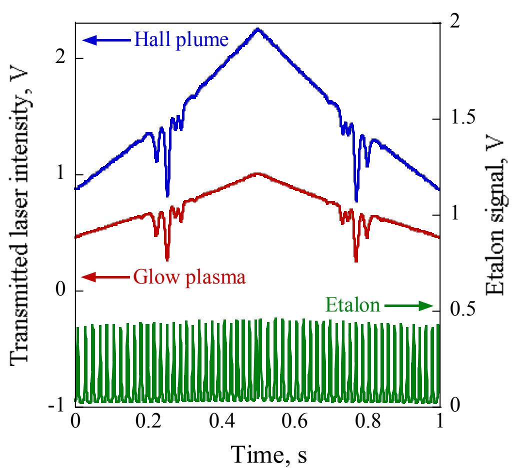

Fig.5 Transmitted laser intensity signals of Hall plume and glow plasma and etalon signal.

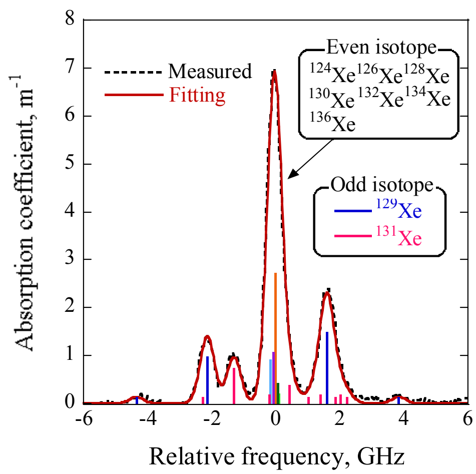

Fig.6 Absorption profile after Abel inversion and curve fitting. (r=20mm, z=50mm)

B. Temperature Distribution

Figure 7 shows a translational temperature distribution of xenon atom. Here, the fitting error is about 50 K. At the channel exit, the temperature is 850 K, whereas it was around 430 K in other region. However, this higher temperature at the exit might be overestimated because of the Zeeman effect. Accurate analysis of the Zeeman effect is difficult, because it consists of anomalous Zeeman splitting of even isotopes, normal Zeeman effect of odd isotopes due to Paschen-Back effect including nuclear spin and relationship between magnetic field and polarization of laser beam. Here, only the anomalous Zeeman effect is discussed as a roughly error estimation. The anomalous Zeeman shift ν_{0_AZ} is expressed as[39],

$$\nu_{0\_AZ} = \mu_B B h^{-1}\left(g_j - g_i\right)M \quad \text{for } \Delta M{=}0$$
$$\nu_{0\_AZ} = \mu_B B h^{-1}\left(g_j M_j - g_i M_i\right) \quad \text{for } \Delta M \pm 1. \qquad (14)$$

The relationship between the magnetic flux density and the anomalous Zeeman shift is shown in Fig.8. Because the magnetic flux density at the channel exit (z=10 mm) is 0.007 T, the overestimation of the Doppler width is less than 0.31 GHz for (M_i,M_j)=(-2,1) and (2,1), which corresponds to 47 % overestimation. Then, the temperature at the channel exit might be close to that of downstream region.

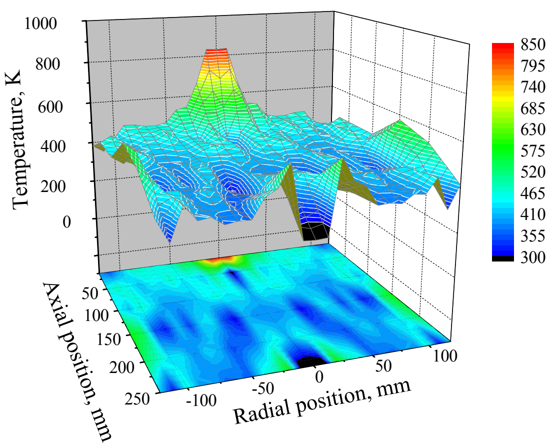

Fig.7 Temperature distribution

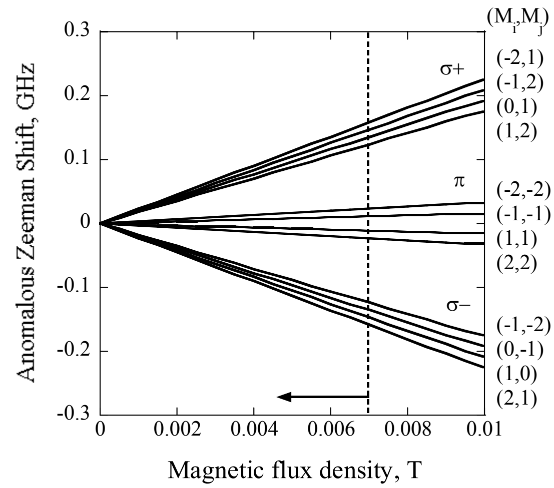

Fig.8 Anomalous Zeeman shift

C. Number Density Distribution

Figure 9 shows a total number density distribution of xenon atom. Here, the Boltzmann equilibrium at T_e=3eV between meta-stable and the other states is assumed, which means that the total number density is 115 times as many as measured meta-stable one. The maximum density is $2.2\text{x}10^{19}\text{m}^{-3}$ at the channel exit. Then, the number density decreases by one-order at z=200 mm.

The number density estimated from mass flow rate, propellant utilization efficiency of 0.8 and channel exit area of 12.1cm^2 is $1.2\ \text{x}10^{19}\text{m}^{-3}$ at the channel exit. Here thermal velocity of xenon atom deduced from the measured translational temperature is used. The higher estimation of a factor of two by laser absorption spectroscopy would be originated from higher population of meta-stable than Boltzmann equilibrium.

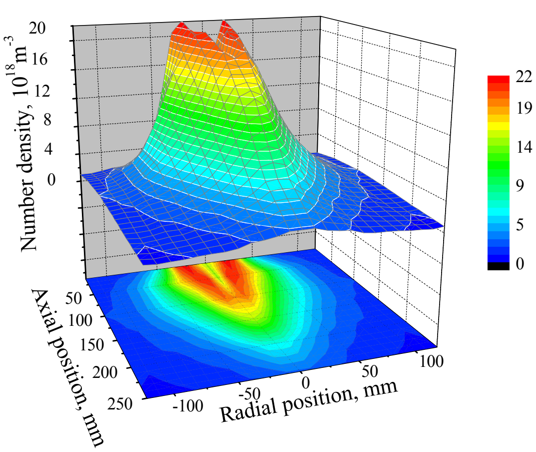

Fig.9 Number density distribution of xenon atom

V. Conclusion

Laser absorption spectroscopy was applied to a magnetic layer type Hall thruster plume using an absorption profile of XeI 823.16nm. The measured profiles after the Abel inversion were fitted by twenty-one Gauss functions considering the isotope shifts and the nuclear spin splitting. The deduced translational temperature was around 430K in the almost all measured region, though it was 850K at the channel exit. However, the higher temperature near the exit might be overestimated by the Zeeman effect. Its maximum error was 47% and then the true temperature would be close to that of downstream. The maximum total number density assuming Boltzmann equilibrium between meta-stable and the other states was $2.2 \times 10^{19} m^{-3}$ at the channel exit. This value is a factor of two higher than that estimated from the mass flow rate and the propellant utilization efficiency. The number density decreased by one order at 200mm away from the exit.

Acknowledgments

This research was partially supported by the Ministry of Education, Science, Sports and Culture, Grant-in-Aid for Research Fellowships of the Japan Society for the Promotion of Science for Young Scientists, 16-10857, 2005.

References

[1]Bober A., Maslennikov, N., Day, M., Popov, G. and Rylov, Yu., “Development and Application of Electric Propulsion Thruster in Russia,” Proceedings of the 23rd International Electric Propulsion Conference, IEPC 93-001, 1993.

[2]Saccoccia, G., “Introduction to the European Activities in Electric Propulsion,” Proceedings of the 28th International Electric Propulsion Conference, IEPC 03-341, 2003.

[3]Blandino, J., “The Year in Review, Electric Propulsion,” Aerospace America, Dec. 2003, pp. 60, 61.

[4]Kim, V., “Main Physical Features and Processes Determining the Performance of Stationary Plasma Thrusters,” Journal of Propulsion and Power, Vol. 14, No. 5, 1998, pp. 736–743.

[5]Kaufman, H. R., “Technology of Closed-Drift Thrusters,” *AIAA Journal*, Vol. 23, No. 1, 1985, pp. 78–86.

[6]Choueiri, E.Y., “Fundamental Difference Between the Two Hall Thruster Variants,” *Physics of Plasmas*, Vol. 8, No. 11, 2001, pp. 5025–5033.

[7]Haas, J. M., Gulczinski, F. S., Gallimore, A> D., Spanjers, G. G., and Spores, R. D., “Performance Characteristics of a 5 kW Laboratory Hall Thruster,” AIAA Paper 98-3503, 1998.

[8]Valentian, D., and Maslennikov, N., “The PPS 1350 Probram,” Proceedings of the 25th International Electric Propulsion Conference, IEPC 97-134, 1997.

[9]Yamamoto, N., Komurasaki, K. and Arakawa, Y., “Discharge Current Oscillation in Hall Thrusters,” *Journal of Propulsion and Power*, Vol. 21, No. 5, 2005, pp. 870-876.

[10]Tahara, H., Goto, D., Yasui, T. and Yoshikawa, T., “Thrust Performance and Plasma Features of Low-Power Hall-Effect Thrusters,” *Vacuum*, Vol. 65, No.3-4, 2002, pp.367-374.

[11]Boyd, I. D., “Review of Hall Thruster Plume Modeling,” *Journal of Spacecraft and Rockets*, Vol. 38, No. 3, 2001, pp.381-387.

[12]King, L. B., Gallimore, A. D., and Marrese, C. M., “Transport-Property Measurements in the Plume of an SPT-100 Hall Thruster,” *Journal of Propulsion and Power*, Vol. 14, No. 3, 1998, pp.327-335.

[13]Tajmar, M., Gonzalez, J., and Hilgers, A., “Modeling of spacecraft-Environment Interactions on SMART-1,” *Journal of Spacecraft and Rockets*, Vol. 38, No. 3, 2001, pp.393-399.

[14]Domonkos, M. T., Gallimore, A. D., Marrese, C. M., and Haas, J. M., “Very-Near-Field Plume Investigation of the Anode Layer Thruster,” *Journal of Propulsion and Power*, Vol. 16, No. 1, 2000, pp.91-98.

[15]King, L. B., and Gallimore, A. D., “Ion-Energy Diagnostics in the Plasma Exhaust Plume of a Hall Thruster,” *Journal of Propulsion and Power*, Vol. 16, No. 5, 2000, pp.916-922.

[16]King, L. B., and Gallimore, A. D., “Mass Spectral Measurements in the Plume of an SPT-100 Hall Thruster,” *Journal of Propulsion and Power*, Vol. 16, No. 6, 2000, pp.1086-1092.

[17]Gulczinski, III, F. S., and Gallimore, A. D., “Near-Field Ion Energy and Species Measurements of a 5-kW Hall Thruster,” *Journal of Propulsion and Power*, Vol. 17, No. 2, 2001, pp.418-427.

[18]Gallimore, A. D., “Near- and Far-Field Characterization of Stationary Plasma Thruster Plumes,” *Journal of Spacecraft and Rockets*, Vol. 38, No. 3, 2001, pp.441-453.

[19]Kim, S. W., and Gallimore, A. D., “Plume Study of a 1.35-kW SPT-100 Using an ExB Probe,” *Journal of Spacecraft and Rockets*, Vol. 39, No. 6, 2002, pp.904-909.

[20]King, L., B., and Gallimore, A. D., “Ion-Energy Diagnostics in an SPT-100 Plume from Thrust Axis to Backflow,” *Journal of Propulsion and Power*, Vol. 20, No. 2, 2004, pp.228-242.

[21]Gonzalez, J., and Estublier, D., “Spacecraft/thrusters interaction analysis for SMART-1,” International Electric Propulsion Conference, IECP-2005-003, 2005.

[22]Taccogna, F., Longo, S., and Capitelli, M., “Particle-in-Cel with Monte Carlo Simulation of SPT-100 Exhaust Plumes,” *Journal of Spacecraft and Rockets*, Vol. 39, No. 3, 2002, pp.409-419.

[23]Oh, D. Y., Hastings, D. E., Marrese, C. M., Haas, J. M., and Gallimore, A. D., "Modeling of Stationary Plasma Thruster Plumes and Implications for Satellite Design," *Journal of Propulsion and Power*, Vol. 15, No. 2, 1999, pp.345-357.

[24]Boyd, I. D., Van Gilder, D. B., and Liu, X., "Monte Carlo Simulation of Neutral Xenon Flows in Electric Propulsion Devices" *Journal of Propulsion and Power*, Vol. 14, No. 6, 1998, pp.1009-1015.

[25]Mikellides, I. G., Jongeward, G. A., Katz, I. and Manzela, D. H., "Plume Modeling of Stationary Plasma Thrusters and Interactions with the Express-A Spacecraft," *Journal of Spacecraft and Rockets*, Vol. 39, No. 6, 2002, pp.894-903.

[26]Matsui, M., Komurasaki, K., and Arakawa, Y., "Laser Absorption Spectroscopy in High Enthalpy Flows," AIAA Paper 05-5325, 2005.

[27]Demtroeder, W., Laser Spectroscopy, 3rd edition, Springer-Verlag, Berlin, 2002.

[28]Deutch, M., "Abel inversion with a simple analytic representation for experimental data," *Applied Physics Letters*, Vol 42, 1983, pp 237-239.

[29]Herzberg, G. H., Atomic Spectra and Atomic Structure, DOVER PUBLICATIONS, New York, 1945.

[30]NIST Atomic Spectra Database: http://physics.nist.gov/cgi-bin/AtData/main_asd

[31]Cedolin, J. R., Hanson, R. K., and Cappelli, M. A., "Semiconductor Laser Diagnostics for Xenon Plasmas," AIAA Paper 94-2739, 1994.

[32]Pfrommer, T., Auweter-Kurtz, M., and Winter, M. W., "Fabry-Perot Interferometry on Xenon for Future Application with Radio-frequency Ion Thrusters (RIT)," Space Technology Education Conference STEC2005, 2005

[33]Mazouffre, S., Pagnon, D., Lasgorceix, P., and Touzeau, M., "Temperature of xenon atoms in a stationary plasma thruster," International Electric Propulsion Conference, IECP-2003, 2003.

[34]Smith, T. B., Ngom, B. B., Linnell, J. A., and Galimore, A. D., "Diode Laser-Induced Fluorescence of Xenon Ion Velocity Distributions," AIAA Paper, AIAA 2005-4406.

[35] Fischer, W., Huhnermann, H., Kromer, G., and Schafer, H. J., "Isotope Shifts in the Atomic Spectrum of Xenon and Nuclear Deformation Effects," Z. Physik, Vol.270, 1974, pp.113.

[36]Jackson, D. A., and Coulombe, M. C., "Isotope shifts in the arc spectrum of xenon," *Proceedings of the Royal Society of London A*, Vol. 338, 1974, pp.277, 298.

[37] Jackson, D. A., and Coulombe, M. C., "Hyperfine structure in the arc spectrum of xenon," *Proceedings of the Royal Society of London A*, Vol. 327, 1972, pp.137, 145.

[38]Geisen, H., Krumpelmann, T., Neuschafer, D., and ttinger, C., "Hyperfine Splitting Measurements on the 6265A and 6507A Lines of Seven Xe Isotopes by LIF on a Beam of Metastable Xe($^3P_{0,2}$) Atoms," *Physics Letters A*, Vol. 130, 1988, pp.299.

[39]Candler, C.C. Atomic Spectra and the Vector Model, Van Nostrand, 1964.